nature neuroscience

ARTICLES

https://doi.org/10.1038/s41593-018-0135-z

# The functional organization of cortical feedback inputs to primary visual cortex

Tiago Marques[1,2], Julia Nguyen[1,2], Gabriela Fioreze[1] and Leopoldo Petreanu[1*]

**Cortical feedback is thought to mediate cognitive processes like attention, prediction, and awareness. Understanding its function requires identifying the organizational logic of feedback axons relaying different signals. We measured retinotopic specificity in inputs from the lateromedial visual area in mouse primary visual cortex (V1) by mapping receptive fields in feedback boutons and relating them to those of neurons in their vicinity. Lateromedial visual area inputs in layer 1 targeted, on average, retinotopically matched locations in V1, but many of them relayed distal visual information. Orientation-selective axons overspread around the retinotopically matched location perpendicularly to their preferred orientation. Direction-selective axons were biased to visual areas shifted from the retinotopically matched position along the angle of their antipreferred direction. Our results show that feedback inputs show tuning-dependent retinotopic specificity. By targeting locations that would be activated by stimuli orthogonal to or opposite to a cell's own tuning, feedback could potentially enhance visual representations in time and space.**

The neocortex is composed of reciprocally connected, hierarchically organized areas[1–3]. Feedback (FB) connections going from higher-order to lower-order cortical areas have been linked to attention, prediction, expectation, and awareness[4–8], but their role in cortical computation is largely unknown. One of the main challenges hampering our understanding of the functional role of FB inputs is that there are no known organizational rules to constrain and inspire theories of FB function. FB axons project diffusely to layer (L)1 and L5/6 of their target area[9] and relay a mixture of functionally diverse signals[10–12]. Theories of hierarchical cortical computation make explicit or implicit predictions about how the diverse signals relayed by FB projections should relate to the functional properties of their postsynaptic targets[13–16]. In visual cortex, this implies relating the tuning properties of the FB axons with the retinotopic location they target in lower visual areas. If FB connections targeted different retinotopic locations depending on the functional properties of the individual axons, they could facilitate many useful visual computations[17]. For example, direction-selective FB axons could innervate neurons in lower areas with receptive fields representing an area in visual space shifted along the same axis as the axon's preferred direction. Such a wiring arrangement would result in predictive FB signals, exciting neurons along the expected trajectory of a moving object. However, it is unclear to what extent FB projections to primary visual cortex (V1) target specific retinotopic areas or functional domains depending on their tuning properties[18–20]. Here we used $Ca^{2+}$ imaging in FB axons[10] and intrinsic signal imaging to measure the tuning-dependent retinotopic specificity of FB inputs from the lateromedial visual area (LM) to L1 of mouse V1. LM contains a retinotopically organized map of the visual field and is one of the major sources of FB inputs to V1[21,22]. We found that FB inputs from LM are functionally organized in V1, with their tuning properties determining the retinotopic locations they innervate.

## Results

**Measuring the retinotopic specificity of LM inputs in L1 of V1.** We identified V1 and the surrounding higher-order visual areas using intrinsic signal imaging (ISI)[22,23] and injected an adeno-associated virus (AAV) encoding GCaMP6s[24] in LM (Fig. 1a,b). The virus infected L2/3 and L5 neurons over an area encompassing most of the LM (600–800 µm in diameter), thus labeling the majority of the LM→V1 FB inputs. Fluorescent axons from GCaMP6s$^+$ neurons formed dense projections in L1 and L5/6, covering the entire extent of V1 (Supplementary Fig. 1). Using a two-photon microscope, we imaged LM axons in many locations across V1 (45 locations, 5 animals; Supplementary Table 1) while presenting visual stimuli to the contralateral eye. GCaMP6s$^+$ axons appeared as bright spots in L1 (Fig. 1c) showing large visually evoked fluorescence transients that likely correspond to presynaptic boutons (Fig. 1d and Supplementary Fig. 2)[10,25–27]. We mapped the receptive fields (RFs) of individual varicosities in L1[28] (Fig. 1d) using small moving bars presented inside a 10° by 10° square. Aided by vasculature landmarks, we compared the RF position of individual varicosities to those of V1 neurons in their vicinity measured by ISI (Fig. 1e–g).

In separate experiments we measured whether ISI reflected the RF position of V1 neurons (Fig. 2). We mapped RFs in 92% (2,459 of 2,673 neurons, 23 imaging locations, 4 mice; Supplementary Table 1) of L2/3 V1 neurons. As expected[23], ISI faithfully tracked the average RF position of V1 neurons (Fig. 2a–e). The difference in visual coordinates from the center of each RF to their retinotopic position in V1, as determined by ISI, defined the displacement ΔRF with components ΔAzimuth and ΔElevation and deviation angle θ (Fig. 1g). The ΔRF values for L2/3 V1 neurons had ΔAzimuth and ΔElevation close to zero, indicating that they closely matched the ISI value at that location (Fig. 2f). However, they were locally diverse in V1, scattering from the intrinsic value by 7.1 ± 1.7° (Methods; $n = 4$ mice), consistent with previous measurements[29,30].

**LM inputs are retinotopically matched but highly scattered.** We mapped RFs in 33% (4,490 of 13,793 varicosities) of LM varicosities in L1 of V1. Consistent with the larger RFs observed in higher visual areas[21], RFs from FB varicosities were larger than those of L2/3 V1 neurons (half short and long axes: LM, 9.35 ± 3.48° and 18.88 ± 7.93°; V1, 8.21 ± 2.27° and 13.88 ± 5.20°; area: LM,

[1]Champalimaud Research, Champalimaud Center for the Unknown, Lisbon, Portugal. [2]These authors contributed equally: Tiago Marques and Julia Nguyen. *e-mail: leopoldo.petreanu@neuro.fchampalimaud.org



© 2018 Nature America Inc., part of Springer Nature. All rights reserved.

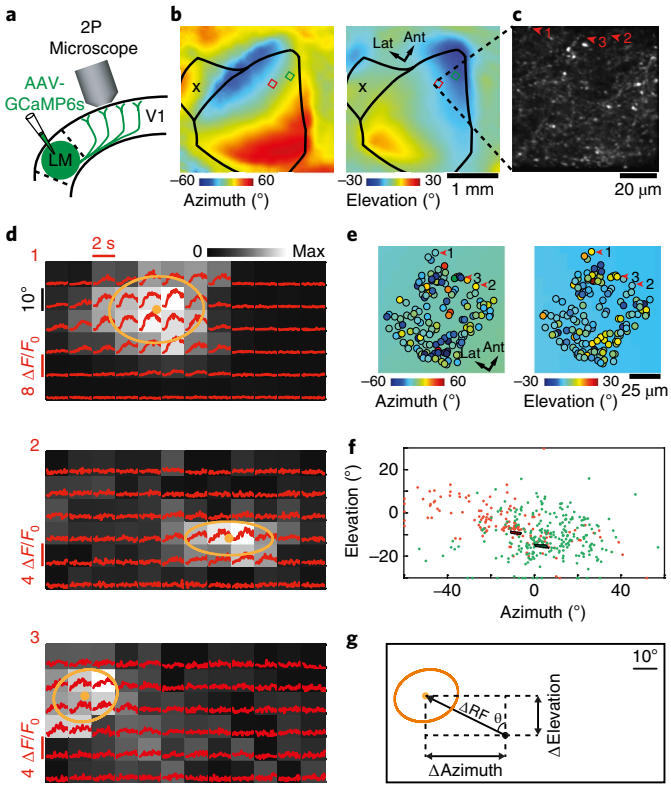


**Fig. 1 | Measuring the retinotopic specificity of LM inputs in L1 of V1.** **a**, LM neurons were infected with GCaMP6s and their axons were imaged in V1. **b**, Retinotopic maps obtained by intrinsic signal imaging (left, azimuth; right, elevation). Cross, injection site; red and green squares, example two-photon imaging field of views (out of 45 fields of view). Lat, lateral; Ant, anterior. **c**, Two-photon field of view (red square in **b**) showing LM axons in L1. Arrowheads, boutons shown in **d**. **d**, RFs of individual LM boutons (3 examples from 4,490 boutons with mapped RFs). Red traces, mean fluorescence signals for stimulus at each of the locations stimulated. Stimulus onset was at the beginning of each trace and lasted for 1 s. Greyscale color map, mean response 0–2 s after stimulus onset. Ellipse, fitted RF; dot, RF center. **e**, LM boutons overlaid over V1 retinotopic maps of **b** (red square). The colors of the circles represent the retinotopic positions of RF centers. Arrowheads, example boutons from **c** and **d**. **f**, RF centers of LM boutons from two imaging sessions located in different positions over V1. Colors correspond to imaging locations in **b**. Filled areas represent the areas of the V1 retinotopic map covered by each field of view. **g**, RF fit and center (orange) from example bouton 3 from **d**. The relative retinotopic position (ΔRF) was defined as the difference between the bouton's RF center and its retinotopic position over V1 (black dot).

$597 \pm 410°^2$; V1 L2/3, $378 \pm 230°^2$; Wilcoxon rank-sum test, $P = 6.6 \times 10^{-117}$). Individual boutons within a single two-photon field of view ($80 \times 80$ µm) responded to stimuli in different positions of the visual field (Fig. 1d–f), suggesting that information from a wide area of visual space converges in L1 of V1. While RF positions in neighboring varicosities showed large variability, the population average varied as a function of their position in the V1 retinotopic map (Figs. 1f and 3a). Both the azimuths and elevations of the boutons' RF centers varied as a function of the retinotopic position in V1 where they were located (linear regression $P = 1.4 \times 10^{-12}$ for azimuth and $P = 1.1 \times 10^{-6}$ for elevation; Fig. 3a). Values of ΔAzimuth and ΔElevation were over-represented around 0 and underrepresented for larger deviations from what would be expected if the RF of LM boutons were independent from their position in V1 (Fig. 3b). The scattering of RFs around the retinotopically matched position was larger in azimuth than in elevation, as observed in L2/3 V1 neurons (Figs. 2f and 3b). This difference could not be attributed to the sampling anisotropy from our rectangular monitor, as it was also observed when restricting analyses to a square stimulus grid (Supplementary Fig. 3).

After correcting for sampling biases (Methods), we obtained the two-dimensional (2D) probability distribution of ΔRF (Fig. 4a,b). Half of the RF centers of LM FB varicosities were within 21° of their retinotopic position in V1 (Fig. 4c). However, varicosities with RFs at distant positions in visual space were abundant (30% > 30° away; Fig. 4c). Dendrites of V1 pyramidal neurons can extend for up to 300 µm in L1, corresponding to 30° over the retinotopic representation in V1[29]. As a consequence, the broad distribution of ΔRF (Fig. 4b) could match the local diversity of RFs of the dendrites in V1. Alternatively, it could reflect the relay of distal visual information to V1 neurons. To distinguish these two hypotheses, we estimated the ΔRF of dendritic segments of V1 neurons by considering the local scatter of V1 somata (from Fig. 4a) and the span of dendritic trees in L1 (Methods). We found that the RF centers of converging LM boutons were from more distant locations than what would be predicted if they matched the RF diversity of V1 dendrites in L1 (Fig. 4c; $P = 2 \times 10^{-4}$, two-sided permutation test; 50% of V1 somatic RF within 8° of their retinotopic position and 50% of dendritic RF within 13° of their retinotopic position). Thus, LM FB is a source of distant visual information to V1 neurons. We estimated the extent of the visual information converging into V1 from LM FB inputs. By considering the visual coverage of individual varicosities' RFs (Fig. 1d) we obtained the 2D distribution of the probability that a given point in relative visual space was represented by one converging LM→V1 input (Fig. 4d). Half of the visual coverage relayed by LM varicosities was more than 24° away from their retinotopic position in V1, with 20% being located more than 40° away (Fig. 4e).

By randomly sampling from the 2D ΔRF probability distributions of V1 somata and LM boutons (Fig. 4a,b), we can estimate the average overlap between the LM boutons and V1 neurons at that position. When taking into account the local diversity of RF positions from V1 neurons or their dendrites in L1, half of the converging LM RFs in L1 showed no overlap with them (Fig. 4f). We estimated the extent of the visual information carried by LM FB as a function of the number of inputs sampled by a V1 neuron in V1 (Fig. 4g). We sampled from the LM ΔRF probability distribution a given number of random of inputs and calculated the aggregate RF. By connecting with a small number of LM inputs, a neuron extending a single dendritic branch to L1 can sample a visual area much larger than the mean V1 RF. The aggregate RF of five LM FB inputs covered, on average, an area more than six times larger than the average V1 RF. This area became even larger when V1 neurons were connected with more LM inputs. Furthermore, the aggregate RF became slightly larger when taking into account the fact that V1 neurons can sample L1 inputs at multiple points through the lateral extent of their apical tufts inputs (Fig. 4g). Thus, LM inputs in L1 of V1 are, on average, retinotopically matched, targeting regions of V1 representing the same location in the visual field. However, there is a broad scattering in the retinotopic specificity of LM→V1 inputs, with a large proportion of them relaying distant visual information to V1 neurons.

**Converging orientation-selective inputs over-represent visual areas orthogonal to their preferred orientation.** We next asked whether the deviations in retinotopic position depended on the tuning properties of LM boutons (Fig. 5). After mapping their RFs, we measured the responses of individual varicosities to oriented drifting gratings. LM axons responded briskly to moving gratings of particular orientations (Fig. 5a). We found varicosities with different preferred orientations intermingled in L1. Of 3,642 varicosities with mapped RFs, 1,718 (47%) were orientation-selective (OS). There was an over-representation of varicosities preferring vertical



© 2018 Nature America Inc., part of Springer Nature. All rights reserved.

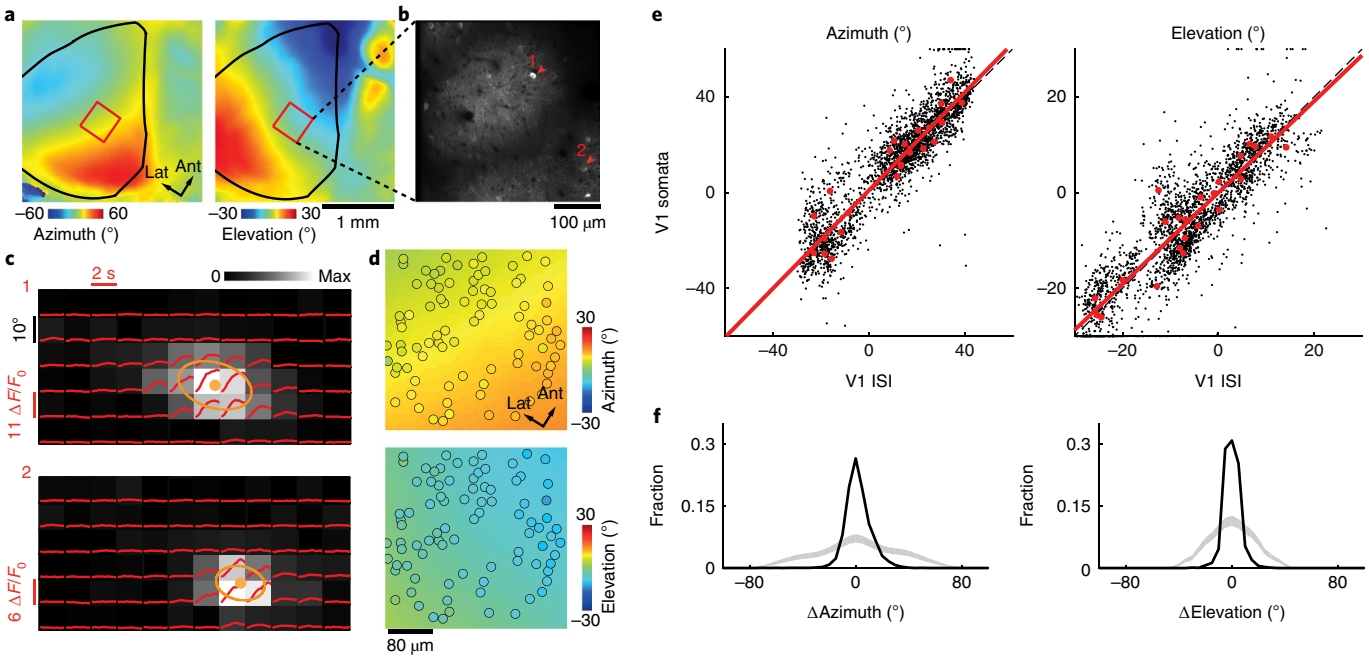


**Fig. 2 | Intrinsic signal imaging reflects the average RF position of V1 neurons. a**, Intrinsic signal retinotopic maps (left, azimuth; right, elevation). Red square represents example two-photon imaging field of view. **b**, Field of view in **a** showing L2/3 V1 neurons. Arrowheads, neurons shown in **c**. **c**, RFs of example L2/3 V1 neurons (2 examples from $n = 2{,}459$ neurons with mapped RFs). Red traces, mean fluorescence signals for stimulus at each of the locations stimulated. Stimulus onset was at the beginning of each trace and lasted for 1 s. Greyscale color map, mean response 0–2 s after stimulus onset. Ellipse, fitted RF; dot, RF center. **d**, L2/3 V1 neurons overlaid over retinotopic maps of **a**. The colors of the circles represent the retinotopic positions of their RF centers. **e**, RF centers of L2/3 V1 neurons versus their position in the ISI retinotopic maps (left, azimuth; right, elevation). Red points, mean values for each imaging location; red lines, linear fits of the mean values (azimuth, $P = 2.1 \times 10^{-11}$; elevation, $P = 1.2 \times 10^{-10}$; $n = 23$ imaging locations) **f**, Probability distribution of ΔRF components ΔAzimuth and ΔElevation of L2/3 V1 neurons. Shading, 95% confidence interval estimated by shuffling V1 ISI values across all cells; $n = 2{,}459$ L2/3 V1 neurons.

orientations, both when counting all OS varicosities (data not shown) or only those with mapped RFs (Fig. 5b). We measured the distribution of the ΔRF deviation angle θ (Fig. 1g) for LM boutons of different preferred orientations using angular bins (Fig. 5c and Supplementary Fig. 4). As there was a general enrichment of boutons located on the horizontal bins (Supplementary Figs. 3 and 4), to isolate orientation-specific effects on the OS ΔRF distributions, we normalized the counts in each bin to those of nonselective boutons (Methods). In these normalized angular histograms plots, varicosities appeared enriched along specific axes depending on their orientation preference (Fig. 5d,e). To see how this enrichment related to the boutons' orientation tuning, we obtained normalized angular counts of deviation angle θ using bowtie-shaped bins (Fig. 5f,g). The preferred orientation of OS boutons defined parallel and perpendicular visual spaces (Fig. 5f). Thus, counts in each bowtie bin measured LM boutons whose RF position deviated along a particular axis relative to the groups' preferred orientation. Averaging these normalized counts across the different OS groups showed that LM boutons were significantly more abundant along the axis perpendicular to their preferred orientation and less frequent along the axis of their preferred orientation than what would be expected by chance (Fig. 5g–i). This enrichment corresponded to 43% more boutons in the perpendicular than in the parallel bin in absolute counts (Supplementary Fig. 4). The enrichment of boutons in the perpendicular axis increased among grating-responsive boutons with orientation selectivity and was largest for boutons located at a ΔRF distance ($\|\Delta RF\|$) from 16° to 30° (Supplementary Fig. 5). The enrichment along the perpendicular axis was observed when direction-selective (DS) boutons were removed from the OS group (Supplementary Fig. 6), indicating that it was independent of any DS-specific effects. This spatial arrangement of OS LM inputs resulted in an increase in probability of ΔRF values in locations along the perpendicular axis (Fig. 5j). Consequently, OS inputs were more likely to encode regions of visual space extending orthogonally to their preferred orientation than nonselective ones (Fig. 5j). This convergence of inputs in V1 indicates that OS LM inputs tend to overspread around the retinotopically matched position orthogonally to their preferred orientation in L1 of V1 (Fig. 5k).

**Converging DS inputs deviate from the matching retinotopic position in the angle of their antipreferred direction.** We then tested the retinotopic specificity of DS boutons. We found 754 (21%) LM varicosities that responded differentially to gratings moving in opposing directions (Fig. 6a). DS boutons preferring gratings moving along the nasal–temporal direction were twice as abundant as those preferring other directions (Fig. 6b). We counted in angular bins and normalized the distribution of the ΔRF deviation angle, θ, as described previously (Fig. 6c,d and Supplementary Fig. 4). We obtained normalized counts in angular bins located at different angles relative to the bouton's preferred direction and averaged them (Fig. 6e,f). The number of DS boutons was selectively enriched in the bin with the same angle as their preferred direction and reduced in the opposite one (Fig. 6f,g). In absolute counts, there were 69% more boutons in the bin corresponding to the preferred direction than to the opposite one (Supplementary Fig. 4). This difference tended to increase with direction selectivity but did not reach significance ($P = 0.13$) and was largest for boutons with a RF mismatch distance ($\|\Delta RF\|$) from 21° to 29° (Supplementary Fig. 5). When compared with nonselective boutons, DS boutons were more likely to represent areas shifted from the matching retinotopy along the



© 2018 Nature America Inc., part of Springer Nature. All rights reserved.

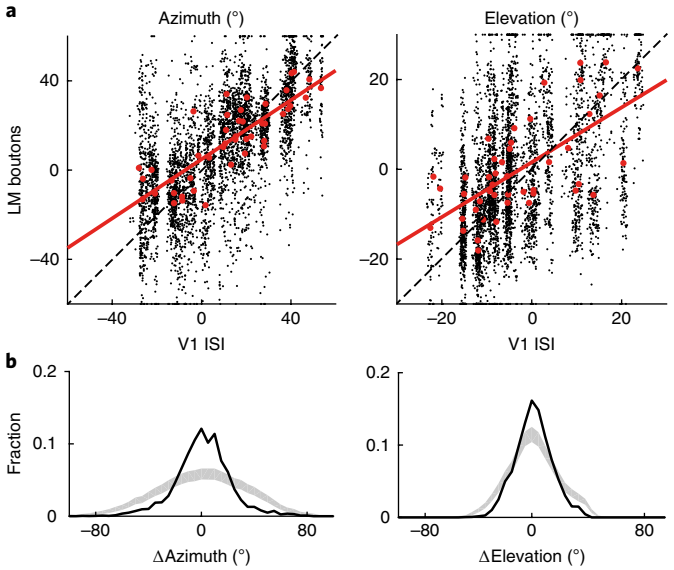


**Fig. 3 | LM inputs in V1 are retinotopically matched but highly scattered.** **a**, RF centers of LM boutons versus their retinotopic positions in V1 (left, azimuth; right, elevation). Red points, mean values for each imaging location; red lines, linear fits of the mean values (azimuth, $P = 1.4 \times 10^{-12}$; elevation, $P = 1.1 \times 10^{-6}$; $n = 45$ imaging locations). Given the large scatter in RF position in LM inputs, deviations were sampled asymmetrically at the extremes, resulting in slopes less steep than unity (dashed line). **b**, Probability distribution of ΔRF components ΔAzimuth and ΔElevation of LM boutons. Shading, 95% confidence interval estimated by shuffling V1 ISI values across all boutons; $n = 4{,}490$ boutons.

preferred direction and less likely to represent areas shifted in the antipreferred one (Fig. 6h). This arrangement of LM inputs resulted in the convergence in V1 of DS inputs over-representing locations lying along the angle of their preferred direction, i.e., positions lying 'ahead' along the trajectory of a moving object. This indicates that LM neurons project 'backwards' to innervate areas in V1 deviating from their matching retinotopic position in the angle of their antipreferred direction (Fig. 6i).

## Discussion

Using axonal calcium imaging, we measured the visual information from LM converging in L1 of V1 and compared it to the RF of neurons in their vicinity. We found that the RFs of LM boutons tended to encode the same regions of the visual field as V1 neurons in their vicinity. However, a large proportion of boutons relayed distal visual information, and the part of the visual field they represented depended on their tuning properties following simple geometric rules.

**Technical considerations.** We estimated the RFs of V1 neurons innervated by FB inputs by relating the bouton's position in the retinotopic map to the average RF of V1 neurons in that location. This is an approximation, given that apical dendrites can extend considerably in L1 and given the local scatter of V1 somata (Fig. 4a and ref. [29]). Thus, an axon in L1 can potentially contact V1 neurons on any point in a cortical patch corresponding to an area of visual space up to 30° in diameter. Thus, the actual ΔRF of connected LM → V1 neurons might be smaller than our measurements if connections show some degree of specificity for neurons with given RFs. Conversely, the actual tuning-dependent connectional biases of FB axons with V1 neurons are likely to be underestimated by the ΔRF measurements based on retinotopic map position (Figs. 5 and 6), as uncertainty on the actual position of postsynaptic RFs introduced by the extent of dendrites in L1 will tend to blur measurements of axis-specific connectional biases.

**LM feedback is retinotopically matched and relays distant information to V1.** Our results show that, as in monkeys[18] and cats[31], FB inputs from higher-order visual areas of the mouse target retinotopically matched areas in V1. Furthermore, we confirmed that this was also true for inputs terminating in L1. Thus, features of cortico–cortical communication are shared between the mouse and species with higher visual acuity, confirming that many aspects of cortical visual processing are conserved across species[28]. Although on average they are retinotopically matched, LM boutons scatter widely, relaying distant visual information to V1 neurons. The scatter of LM boutons' RFs in V1 was larger than the expected local diversity of V1 dendrites, even when assuming dendritic trees spanning 300 µm (Fig. 4c), an overestimation given that most neurons in V1 extend narrower dendritic arbors to L1. Thus, LM FB is likely to be relaying information from distal visual locations to postsynaptic V1 neurons. Additionally, a small number of converging LM inputs represent visual areas much larger than the average RF of V1 neurons (Fig. 4g), suggesting that these connections could modulate V1 responses[9] depending on contextual information spanning large areas of the visual field. Distant information deviating along the azimuth was more widely available to V1 neurons than information deviating in elevation (Fig. 3 and Supplementary Fig. 3). The origin of this bias could be due to several reasons. The RFs of V1 neurons show a similar arrangement, being more scattered locally along the azimuth than in elevation (Supplementary Fig. 3). Thus, if LM inputs show specificity for connecting with V1 neurons depending on their RF, they would also scatter more in azimuth. However, the local scatter of soma and dendrites cannot account for the full magnitude of the ΔRF variability (Fig. 4c). Another factor is the general bias of FB inputs representing vertically oriented stimuli or temporal–nasal motion, which is predicted to increase the population ΔRF scatter along the horizontal axis (Figs. 5 and 6). However, the anisotropic ΔRF distribution remained significant even after restricting the analysis to isotropically tuned, nonselective boutons ($P = 0.048$; Supplementary Fig. 3), suggesting that the tuning bias of the LM population was not the only factor contributing to the larger deviations in azimuth. Finally, LM as a whole represents an area of visual space spanning more widely in azimuth than in elevation[22,32]. Thus, the larger availability of FB inputs in V1 deviating more along azimuth than in elevation might reflect the anisotropic extent of the visual field represented by the source region. These three factors are not mutually exclusive and might add up, contributing to the anisotropy in the extent of the visual information converging from LM in V1.

**Tuning dependent biases of FB innervation in V1 and functional implications.** A large fraction of FB boutons was tuned for the orientation or direction of moving gratings. Like neurons in V1[33], LM inputs in V1 over-represented temporal–nasal motion, suggesting a specialization of the mouse visual cortex, including its FB connections, for processing the predominant direction experienced during locomotion, given their laterally positioned eyes (Fig. 6b). We found that the retinotopic specificity of LM inputs to V1 depended on their orientation selectivity. There have been conflicting reports of OS-dependent specificity in cortico–cortical FB from V2 to V1 in macaques[18,20] and owl monkeys[19]. We found that OS-specific LM inputs in mouse V1 overextended orthogonally to their preferred orientation, an arrangement found in corticothalamic FB in macaques[34]. In several species, including mice, local horizontal connections show an anisotropic spread in V1, extending preferentially along the axis of their preferred orientation[35–38], where they contact iso-oriented neurons[36,38,39]. This anatomical arrangement of horizontal connections is thought to enhance responses to collinear contour elements[38,40,41]. The rules organizing the retinotopic spread of OS inputs from LM are the opposite of those found in horizontal connections, suggesting that the projections are not involved in directly facilitating V1 responses to flanking collinear



© 2018 Nature America Inc., part of Springer Nature. All rights reserved.

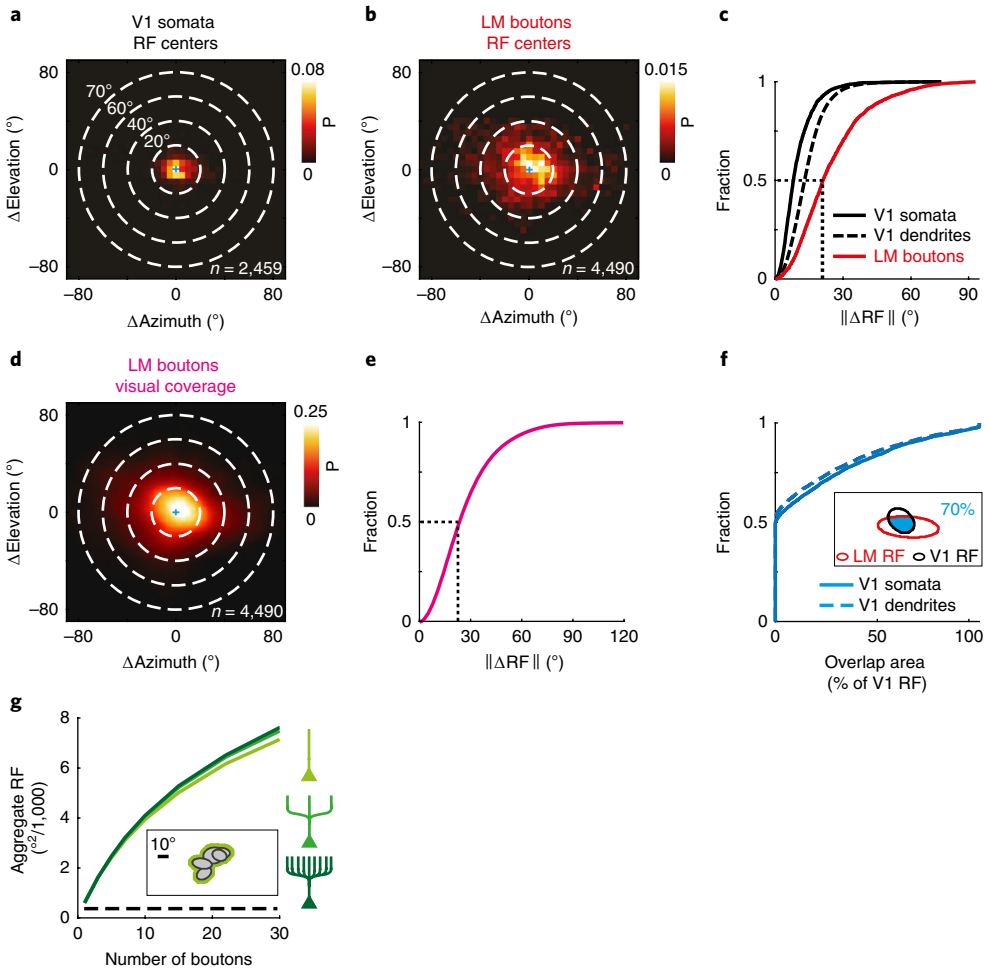


**Fig. 4 | LM inputs relays distal visual information to V1 neurons. a**, 2D probability distribution of ΔRF for L2/3 somata (from data in Fig. 2e). White circles correspond to different ΔRF distances. **b**, 2D probability distribution of ΔRF for LM boutons (from data in Fig. 3a). **c**, Cumulative distribution of ||ΔRF|| of L2/3 somata (black trace, from **a**); V1 dendrites, assuming 300-µm-wide dendritic arbors (dashed trace, from **a**; see Methods); or LM boutons (red trace, from **b**; median 21°). **d**, 2D probability distribution of the visual extent of converging LM inputs in V1. It measures the probability of a LM bouton RF to include a point in visual space in ΔRF coordinates. **e**, Cumulative distribution of the distance of the visual inputs represented by converging LM axons to their location in V1 (from **d**; median 24°). **f**, Cumulative distribution of the LM–V1 RF overlap obtained after sampling 10,000 pairs from the probability distributions in **a** and **b**. Inset: example sampled pair; overlap in blue. Filled line, RF overlap with V1 somata; dashed line, RF overlap when taking into account the extent of V1 dendritic arbors (assuming 300-µm-wide dendritic arbors). **g**, Aggregate RF as a function of the total number of LM boutons sampled from **b**, calculated for neurons sampled at one, three, or nine points in L1 through branches in a 300-µm-wide dendritic tree. Inset: example iteration with 5 boutons (black lines, individual RFs; gray area, aggregate RF; green line, outer perimeter). Dashed line; average RF area of L2/3 neurons.

segments in the mouse. LM inputs contact both pyramidal neurons and interneurons in V1[42]. The net effect of FB on pyramidal neurons can be either excitatory or inhibitory depending on the subtypes of interneurons they engage[5,43]. Thus, FB boutons spreading orthogonally to the axon's preferred orientation could be suppressing activity in their target areas. The combination of collinear excitation, which would be mediated by horizontal connections, with inhibition in orthogonal locations, which would be mediated by cortical FB, could facilitate contour detection as shown in models of V1[44]. Similarly, DS inputs from LM could enhance motion representations in the time domain. As higher-order visual areas respond with a delay to visual stimuli relative to V1[45], DS FB from LM could suppress V1 neurons representing previous positions of a moving object sharpening the temporal profile of V1 responses.

In predictive coding models of hierarchical visual processing, FB afferents relay predictions to lower areas[13–15]. Edges in natural images tend to be long and smooth, with the presence of oriented segments predicting flanking collinear ones[38,46,47]. The connectivity of OS LM inputs in V1 is consistent with these theories, in that FB could be encoding spatial predictions to V1, but it would be doing so by targeting regions that lie orthogonally to those expected to be coactive with them. A similar interpretation is consistent with the arrangement of the DS LM inputs in V1. DS activity predicts that areas shifted along the preferred direction in the retinotopic map should become active shortly after. DS inputs, on the contrary, are biased toward V1 locations lying in the opposite direction. Predictive coding models also propose that predictions relayed by FB connections are compared with bottom-up input in the target area, cancelling expected stimuli. The anatomical arrangement we observed is not consistent with this tenet, as FB inputs did not have biases toward the expected coactive sites but rather to those lying orthogonally (for OS axons) or in opposite direction (for DS axons).

The organizing rules observed in the LM projection could potentially be generalized for FB inputs from other areas given the modularity of cortical circuits. Many visual and nonvisual areas



© 2018 Nature America Inc., part of Springer Nature. All rights reserved.

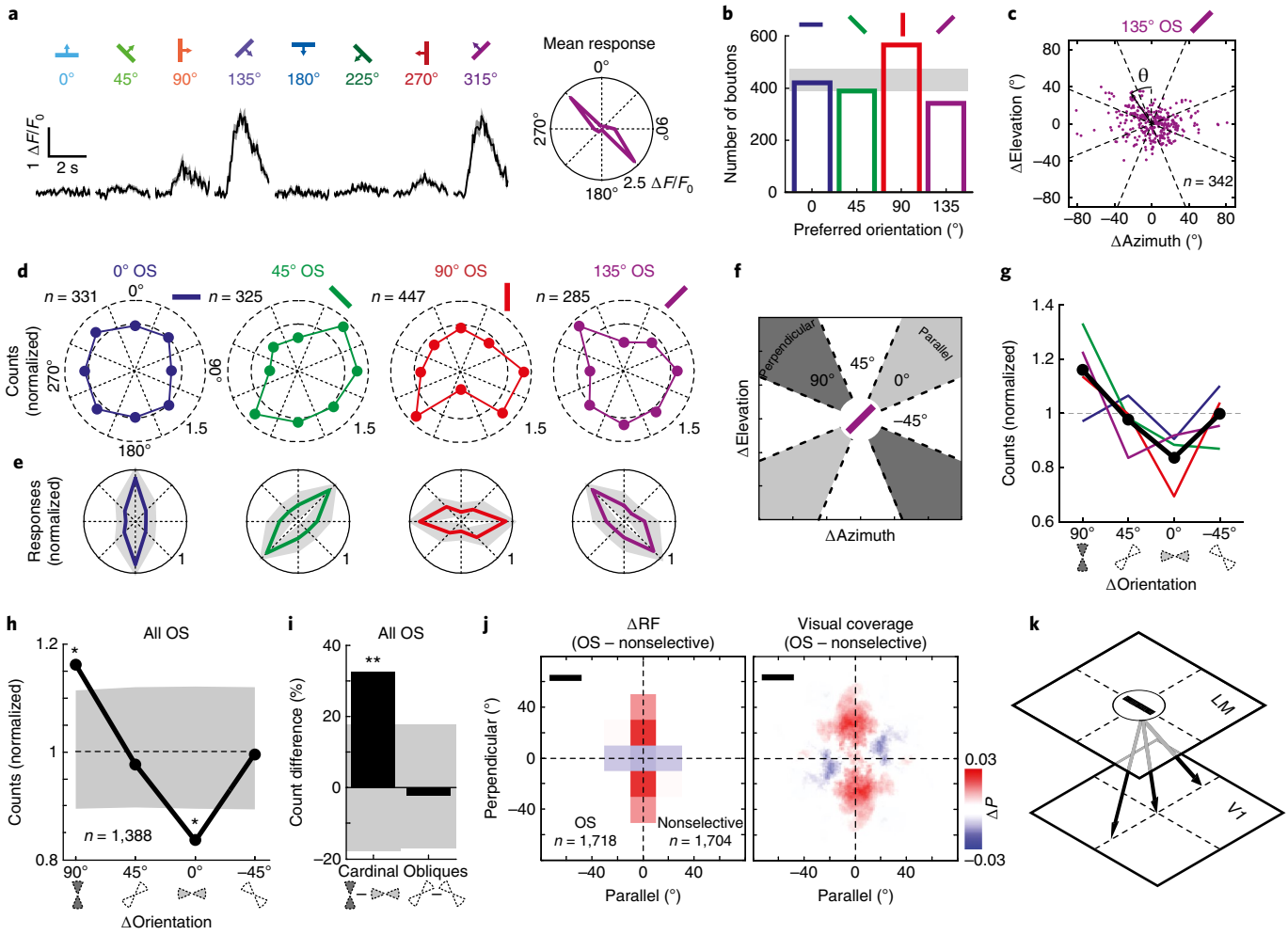


**Fig. 5 | OS FB inputs over-represent visual areas perpendicular to their preferred orientation. a**, Left: mean fluorescence signals of one example OS LM bouton (of 1,718 OS boutons) for gratings stimuli moving in 8 directions. Shading, s.e.m. Right: tuning curve of the same bouton. **b**, Distribution of preferred orientations for OS boutons. Only boutons with measured RF are shown. Shading, 95% confidence interval obtained by resampling from a uniform probability distribution. **c**, ΔRF plot for the 135° OS boutons. Dashed lines, angular bins used to calculate the distribution of the deviation angle, θ. **d**, Angular bin counts of θ for subpopulations of boutons of different preferred orientations. Counts are normalized to nonselective boutons. Boutons with ||ΔRF|| < 10° were discarded for angular counts (Methods). Inner circle = 1. **e**, Mean tuning curves for the subpopulations of OS boutons in **d**. Shading, s.d. **f**, The preferred orientation defines parallel, perpendicular, and oblique bowtie bins. ΔOrientation angles between the bin angle and the bouton's preferred orientation are indicated on each bin. **g**, Colored lines, counts using bowtie bins defined in **f** for the OS subpopulations, normalized to the nonselective population. Line colors correspond to **d**. Black line and circles, weighted mean of the OS subpopulations. Bowtie bin colors correspond to **f**. **h**, Mean normalized bowtie counts for all OS boutons, as in **g** (0°, $^{*}P = 0.013$; 90°, $^{*}P = 0.013$, two-sided permutation test, corrected for multiple comparisons, $n = 1{,}388$ OS boutons and 1,362 nonselective boutons). **i**, Difference in bouton abundance across perpendicular bowtie bins ($^{**}P = 8 \times 10^{-4}$, two-sided permutation test, corrected for multiple comparisons). Shading in **h** and **i**, 95% CI obtained by reshuffling group identities. **j**, Differences in the 2D probability distribution of ΔRF (left; analogous to Fig. 4b) or visual extent probability (right; analogous to Fig. 4d) between OS and nonselective boutons. Bar, preferred orientation. **k**, Tuning-dependent wiring biases of OS LM inputs to V1 consistent with observations in **h**–**j**. Planes represent retinotopic maps in V1 and LM. Bar represents preferred orientation of the LM neurons.

send FB to V1 neurons tuned for orientation and motion direction[48–50] that could potentially be arranged similarly to the LM ones. Such a rule might also not be limited to FB projections tuned to moving edges. FB projections linking areas tuned for more complex features might tend to contact neurons harboring orthogonal or opposite representations to those expected to be coactive with them in the relevant feature space. However, such wiring biases in axons relaying complex representations might not always result in simple geometrical arrangements of FB inputs, as the relevant feature might not be represented in a map in the target area. While a large fraction of LM inputs was tuned to moving oriented edges, the possibility remains that the most relevant selectivity of these inputs was not probed with these simple stimuli. The tuning-dependent geometric arrangement of LM inputs in V1 could in this case reflect relationships between LM inputs and the low-level features encoded by V1 neurons.

Future experiments should determine to what extent the rules observed here for LM inputs in V1 also apply for projections from other areas. Further quantitative descriptions of the signals relayed by FB and its organizing rules will help constrain and inspire theories of hierarchical cortical processing.

## Methods

Methods, including statements of data availability and any associated accession codes and references, are available at https://doi.org/10.1038/s41593-018-0135-z.



© 2018 Nature America Inc., part of Springer Nature. All rights reserved.

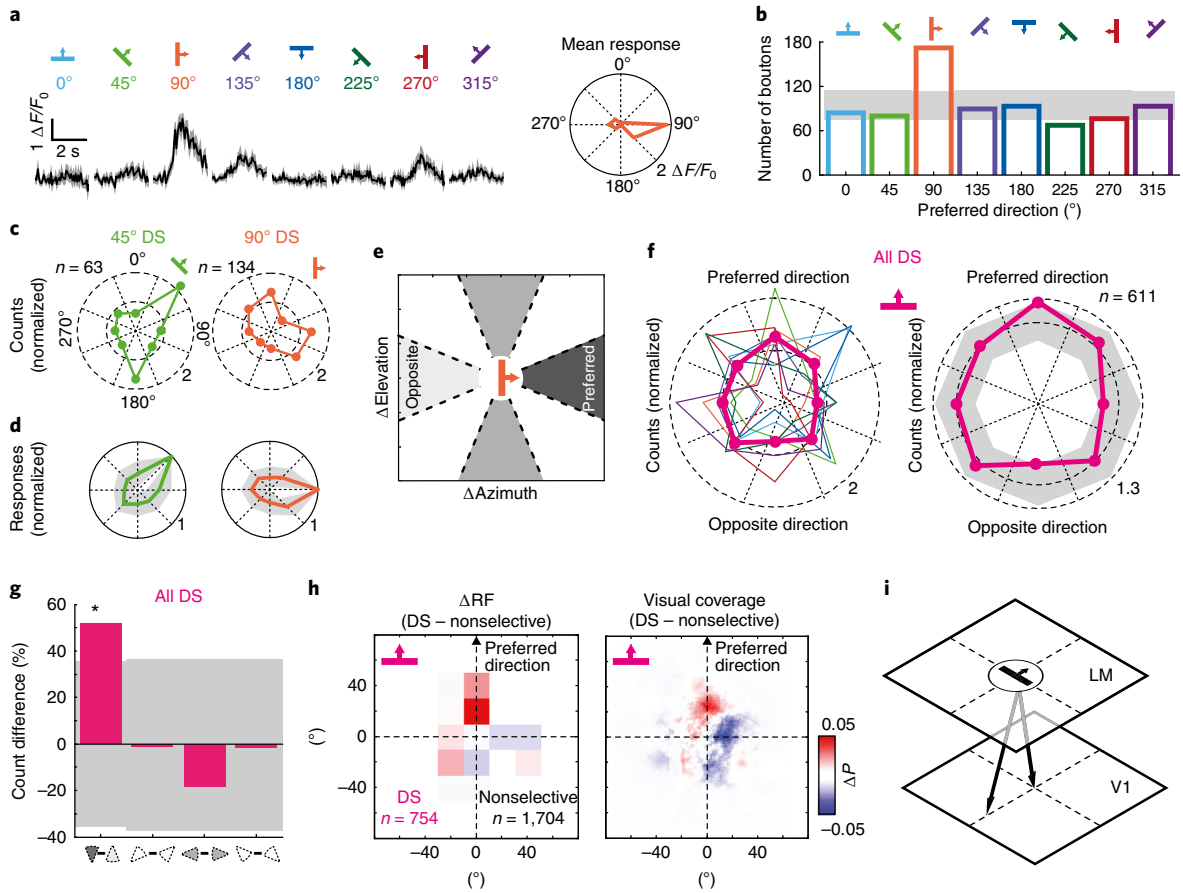


**Fig. 6 | DS FB inputs over-represent visual areas along their preferred motion direction. a**, Left: mean fluorescence signals of one example DS LM bouton (of 754 DS boutons) for gratings stimuli moving in eight directions. Shading, s.e.m. Right: tuning curve of the same bouton. **b**, Distribution of preferred directions for DS boutons. Only boutons with measured RF are shown. Shading, 95% confidence interval obtained by resampling from a uniform probability distribution. **c**, Normalized angular bin counts of θ for boutons selective for 45° and 90° moving gratings. Inner circle = 1. **d**, Mean tuning curves for DS subpopulations in **c**. Shading, s.d. **e**, The bouton's preferred direction defines angular bins lying at different angles from their preferred direction. **f**, Left: thin colored lines show normalized angular counts for the DS subpopulations using the bins defined in **e**. Line colors correspond to **b**. Thick magenta line and dots show weighted mean of the DS subpopulations. Inner circle = 1. Number of boutons in each group: 0°, $n = 69$; 45°, $n = 63$; 90°, $n = 134$; 135°, $n = 71$; 180°, $n = 74$; 225°, $n = 56$; 270°, $n = 62$; 315°, $n = 82$. Right: weighted mean of the DS subpopulations with 95% confidence intervals (shading) obtained by reshuffling group identities; $n = 611$ DS boutons and 1,362 nonselective boutons. **g**, Difference in bouton abundance between angular bins of opposing angles for DS boutons. Angular bin colors correspond to **e**. Shading, 95% confidence intervals obtained by reshuffling group identities (*$P = 0.019$, two-sided permutation test, corrected for multiple comparisons). **h**, Differences in the 2D probability distribution of ΔRF (left) or visual extent probability (right) between DS and nonselective boutons. **i**, Tuning-dependent wiring biases of DS LM inputs to V1 consistent with observations in **f**–**h**. Planes represent retinotopic maps in V1 and LM. Bar with arrow represents preferred direction of the LM neurons.

Received: 1 December 2017; Accepted: 6 March 2018;
Published online: 16 April 2018

## References

1. Felleman, D. J. & Van Essen, D. C. Distributed hierarchical processing in the primate cerebral cortex. *Cereb. Cortex* **1**, 1–47 (1991).
2. Zingg, B. et al. Neural networks of the mouse neocortex. *Cell* **156**, 1096–1111 (2014).
3. Oh, S. W. et al. A mesoscale connectome of the mouse brain. *Nature* **508**, 207–214 (2014).
4. Larkum, M. A cellular mechanism for cortical associations: an organizing principle for the cerebral cortex. *Trends Neurosci.* **36**, 141–151 (2013).
5. Zhang, S. et al. Selective attention. Long-range and local circuits for top-down modulation of visual cortex processing. *Science* **345**, 660–665 (2014).
6. Manita, S. et al. A top-down cortical circuit for accurate sensory perception. *Neuron* **86**, 1304–1316 (2015).
7. Gilbert, C. D. & Li, W. Top-down influences on visual processing. *Nat. Rev. Neurosci.* **14**, 350–363 (2013).
8. Roelfsema, P. R. & de Lange, F. P. Early visual cortex as a multiscale cognitive blackboard. *Annu. Rev. Vis. Sci.* **2**, 131–151 (2016).
9. Angelucci, A. & Bressloff, P. C. Contribution of feedforward, lateral and feedback connections to the classical receptive field center and extra-classical receptive field surround of primate V1 neurons. *Prog. Brain Res.* **154**, 93–120 (2006).
10. Petreanu, L. et al. Activity in motor-sensory projections reveals distributed coding in somatosensation. *Nature* **489**, 299–303 (2012).
11. Makino, H. & Komiyama, T. Learning enhances the relative impact of top-down processing in the visual cortex. *Nat. Neurosci.* **18**, 1116–1122 (2015).
12. Kwon, S. E., Yang, H., Minamisawa, G. & O'Connor, D. H. Sensory and decision-related activity propagate in a cortical feedback loop during touch perception. *Nat. Neurosci.* **19**, 1243–1249 (2016).
13. Rao, R. P. & Ballard, D. H. Predictive coding in the visual cortex: a functional interpretation of some extra-classical receptive-field effects. *Nat. Neurosci.* **2**, 79–87 (1999).
14. Mumford, D. On the computational architecture of the neocortex. II. The role of cortico-cortical loops. *Biol. Cybern.* **66**, 241–251 (1992).
15. Bastos, A. M. M. A. M. et al. Canonical microcircuits for predictive coding. *Neuron* **76**, 695–711 (2012).
16. Brosch, T., Neumann, H. & Roelfsema, P. R. Reinforcement learning of linking and tracing contours in recurrent neural networks. *PLoS Comput. Biol.* **11**, e1004489 (2015).



© 2018 Nature America Inc., part of Springer Nature. All rights reserved.

17. Barlow, H. B. Why have multiple cortical areas? *Vision Res.* **26**, 81–90 (1986).
18. Angelucci, A. & Bullier, J. Reaching beyond the classical receptive field of V1 neurons: horizontal or feedback axons? *J. Physiol. Paris* **97**, 141–154 (2003).
19. Shmuel, A. et al. Retinotopic axis specificity and selective clustering of feedback projections from V2 to V1 in the owl monkey. *J. Neurosci.* **25**, 2117–2131 (2005).
20. Stettler, D. D., Das, A., Bennett, J. & Gilbert, C. D. Lateral connectivity and contextual interactions in macaque primary visual cortex. *Neuron* **36**, 739–750 (2002).
21. Wang, Q. & Burkhalter, A. Area map of mouse visual cortex. *J. Comput. Neurol* **502**, 339–357 (2007).
22. Garrett, M. E., Nauhaus, I., Marshel, J. H. & Callaway, E. M. Topography and areal organization of mouse visual cortex. *J. Neurosci.* **34**, 12587–12600 (2014).
23. Kalatsky, V. A. & Stryker, M. P. New paradigm for optical imaging: temporally encoded maps of intrinsic signal. *Neuron* **38**, 529–545 (2003).
24. Chen, T.-W. et al. Ultrasensitive fluorescent proteins for imaging neuronal activity. *Nature* **499**, 295–300 (2013).
25. Glickfeld, L. L., Andermann, M. L., Bonin, V. & Reid, R. C. Cortico-cortical projections in mouse visual cortex are functionally target specific. *Nat. Neurosci.* **16**, 219–226 (2013).
26. Cox, C. L., Denk, W., Tank, D. W. & Svoboda, K. Action potentials reliably invade axonal arbors of rat neocortical neurons. *Proc. Natl Acad. Sci. USA* **97**, 9724–9728 (2000).
27. Koester, H. J. & Sakmann, B. Calcium dynamics associated with action potentials in single nerve terminals of pyramidal cells in layer 2/3 of the young rat neocortex. *J. Physiol. (Lond.)* **529**, 625–646 (2000).
28. Niell, C. M. & Stryker, M. P. Highly selective receptive fields in mouse visual cortex. *J. Neurosci.* **28**, 7520–7536 (2008).
29. Bonin, V., Histed, M. H., Yurgenson, S. & Reid, R. C. Local diversity and fine-scale organization of receptive fields in mouse visual cortex. *J. Neurosci.* **31**, 18506–18521 (2011).
30. Smith, S. L. & Häusser, M. Parallel processing of visual space by neighboring neurons in mouse visual cortex. *Nat. Neurosci.* **13**, 1144–1149 (2010).
31. Salin, P. A., Girard, P., Kennedy, H. & Bullier, J. Visuotopic organization of corticocortical connections in the visual system of the cat. *J. Comp. Neurol.* **320**, 415–434 (1992).
32. Zhuang, J. et al. An extended retinotopic map of mouse cortex. *eLife* **6**, 1–29 (2017).
33. Hillier, D. et al. Causal evidence for retina-dependent and -independent visual motion computations in mouse cortex. *Nat. Neurosci.* **20**, 960–968 (2017).
34. Murphy, P. C., Duckett, S. G. & Sillito, A. M. Feedback connections to the lateral geniculate nucleus and cortical response properties. *Science* **286**, 1552–1554 (1999).
35. Schmidt, K. E., Goebel, R., Löwel, S. & Singer, W. The perceptual grouping criterion of colinearity is reflected by anisotropies of connections in the primary visual cortex. *Eur. J. Neurosci.* **9**, 1083–1089 (1997).
36. Bosking, W. H., Zhang, Y., Schofield, B. & Fitzpatrick, D. Orientation selectivity and the arrangement of horizontal connections in tree shrew striate cortex. *J. Neurosci.* **17**, 2112–2127 (1997).
37. Sincich, L. C. & Blasdel, G. G. Oriented axon projections in primary visual cortex of the monkey. *J. Neurosci.* **21**, 4416–4426 (2001).
38. Iacaruso, M. F., Gasler, I. T. & Hofer, S. B. Synaptic organization of visual space in primary visual cortex. *Nature* **547**, 449–452 (2017).
39. Gilbert, C. D. & Wiesel, T. N. Columnar specificity of intrinsic horizontal and corticocortical connections in cat visual cortex. *J. Neurosci.* **9**, 2432–2442 (1989).
40. Kapadia, M. K., Ito, M., Gilbert, C. D. & Westheimer, G. Improvement in visual sensitivity by changes in local context: parallel studies in human observers and in V1 of alert monkeys. *Neuron* **15**, 843–856 (1995).
41. Chisum, H. J., Mooser, F. & Fitzpatrick, D. Emergent properties of layer 2/3 neurons reflect the collinear arrangement of horizontal connections in tree shrew visual cortex. *J. Neurosci.* **23**, 2947–2960 (2003).
42. Yang, W., Carrasquillo, Y., Hooks, B. M., Nerbonne, J. M. & Burkhalter, A. Distinct balance of excitation and inhibition in an interareal feedforward and feedback circuit of mouse visual cortex. *J. Neurosci.* **33**, 17373–17384 (2013).
43. Jiang, X., Wang, G., Lee, A. J., Stornetta, R. L. & Zhu, J. J. The organization of two new cortical interneuronal circuits. *Nat. Neurosci.* **16**, 210–218 (2013).
44. Li, Z. A neural model of contour integration in the primary visual cortex. *Neural Comput.* **10**, 903–940 (1998).
45. Polack, P.-O. & Contreras, D. Long-range parallel processing and local recurrent activity in the visual cortex of the mouse. *J. Neurosci.* **32**, 11120–11131 (2012).
46. Sigman, M., Cecchi, G. A., Gilbert, C. D. & Magnasco, M. O. On a common circle: natural scenes and gestalt rules. *Proc. Natl Acad. Sci. USA* **98**, 1935–1940 (2001).
47. Geisler, W. S. Visual perception and the statistical properties of natural scenes. *Annu. Rev. Psychol.* **59**, 167–192 (2008).
48. Marshel, J. H., Garrett, M. E., Nauhaus, I. & Callaway, E. M. Functional specialization of seven mouse visual cortical areas. *Neuron* **72**, 1040–1054 (2011).
49. Andermann, M. L., Kerlin, A. M., Roumis, D. K., Glickfeld, L. L. & Reid, R. C. Functional specialization of mouse higher visual cortical areas. *Neuron* **72**, 1025–1039 (2011).
50. Murakami, T., Yoshida, T., Matsui, T. & Ohki, K. Wide-field Ca(2+) imaging reveals visually evoked activity in the retrosplenial area. *Front. Mol. Neurosci.* **8**, 20 (2015).

## Acknowledgements

We thank C. Harvey, G. De Polavieja, A. Renart, B. Attalah, E. Chiappe, H. Young, and M. Fridman for critical comments on the manuscript. This work was supported by fellowships from Fundação para a Ciência e a Tecnologia to T.M and G.F., Marie Curie (PCIG12-GA-2012-334353) and Human Frontier Science Program (RGY0085/2013) grants to L.P., and by the Champalimaud Foundation.

## Author contributions

T.M., J.N., and L.P. conceived the study. J.N. performed the experiments. T.M. set up and optimized intrinsic signal imaging experiments and visual stimuli. T.M. and L.P. analyzed the data. L.P. built the two-photon microscope. G.F. did histology. T.M., J.N., and L.P. wrote the paper.

## Competing interests

The authors declare no competing financial interests.

## Additional information

**Supplementary information** is available for this paper at https://doi.org/10.1038/s41593-018-0135-z.

**Reprints and permissions information** is available at www.nature.com/reprints.

**Correspondence and requests for materials** should be addressed to L.P.

**Publisher's note:** Springer Nature remains neutral with regard to jurisdictional claims in published maps and institutional affiliations.



© 2018 Nature America Inc., part of Springer Nature. All rights reserved.

## Methods

**Animals.** All procedures were reviewed and approved by the Champalimaud Centre for the Unknown Ethics Committee and performed in accordance with the Portuguese Direcção Geral de Veterinária. Wild-type male C57BL/6J mice were used for in vivo functional imaging of LM FB axons. L2/3 somata in V1 were imaged in one Thy1-GCaMP6s GP4.3 mouse[51] (Jackson Laboratory stock no: 024275) and three C57BL/6J male mice. Mice were individually housed on a reversed light–dark cycle with ad libitum access to food and water and were only used for the experiments reported here.

**Chronic window implantation.** Surgeries were performed on adult mice (8 to 10 weeks old) under isoflurane anesthesia. Bupivacaine (0.05%; injected under the scalp) and Dolorex (1 mg/kg; injected subcutaneously) provided local and general analgesia. Eyes were protected and kept moist using ophthalmic ointment (Clorocil, Laboratório Edol). A circular craniotomy was performed over the left visual cortex (diameter: 4 mm). The dura was left intact. An imaging window was constructed from two layers of microscope cover glass (Fisher Scientific, no. 1 and no. 2) joined with a UV-curable optical glue[10]. The window was embedded into the craniotomy and secured in place using black dental cement. A custom-designed iron headpost was attached to the skull with dental acrylic.

**Intrinsic signal imaging.** Four days after cranial window implantation, intrinsic signal imaging was used to obtain retinotopic maps of the primary visual cortex and surrounding visual areas[22,23,48]. Mice were headfixed and lightly anesthetized with isoflurane (1%) and injected intramuscularly with chlorprothixene (1 mg/kg)[23]. The eyes were coated with a thin layer of silicone oil (Sigma-Aldrich) to ensure optical clarity during visual stimulation. Optical images of cortical intrinsic signals were recorded using a Retiga QIClick camera (QImaging) controlled using Ephus[52] with a high magnification zoom lens (Thorlabs) focused at the brain surface under the glass window at 5 Hz. To measure intrinsic hemodynamic responses, the surface of the cortex was illuminated with a 620-nm red LED while drifting bar stimuli were presented to the right eye in a carefully aligned monitor (see below). An image of the cortical vasculature under the window was obtained using a 535-nm green LED.

**Viral injections.** We targeted virus injections to visual area LM using retinotopic maps obtained by intrinsic signal imaging[22,48]. A small hole was made in the imaging window, allowing access to LM. Virus expressing GCaMP6s (AAV1-Syn-flex-GCaMP6s-WPRE-SV40, University of Pennsylvania Gene Therapy Program Vector Core) was injected (50 nL total, 10 nL/min, 250 and 550 µm deep) into the center of LM, using beveled glass pipettes (Drummond) with diameters of 15–20 µm. Pipettes were backfilled with mineral oil and frontloaded with viral suspension immediately before injection, and virus was injected using a custom volumetric injection system based on a Narishige MO-10 manipulator[10]. To label V1 neurons, virus expressing GCaMP6s (AAV1-Syn-flex-GCaMP6s-WPRE-SV40, University of Pennsylvania Gene Therapy Program Vector Core) was injected into four locations in V1 (30 nL per location, 120 nL total, 10 nL/min, 200–315 µm deep). To prevent backflow during withdrawal, the pipette was kept in the brain for over 5 min before the pipette was pulled up.

**Two-photon imaging.** Imaging was performed 2–5 weeks postinjection. We used a custom microscope (based on the MIMMS design, Janelia Research Campus, https://www.janelia.org/open-science/mimms) equipped with a resonant scanner. Mice were headfixed and anesthetized with isoflurane (0.7–1%) and injected intramuscularly with chlorprothixene (1 mg/kg). The eyes were coated with a thin layer of silicone oil. Visual stimuli were presented to the right eye in a carefully aligned monitor (see below). O-rings were glued to the headpost, concentric with the center of the cranial window, to form a well for imaging. To prevent stray light from the monitor from entering the imaging well, a flexible, conical light shield was attached to the headpost and secured around the imaging objective. GCaMP6s was excited using a Ti:sapphire laser (Chameleon Ultra II, Coherent) tuned to 1,000 nm when imaging axons or 920 nm when imaging somata in L2/3. We used GaAsP photomultiplier tubes (10770PB-40,Hamamatsu) and a 16× (0.8 NA) objective (Nikon). For axonal recordings, the field of view was 80 × 80 µm (512 × 512 pixels), imaged at 15 Hz. For somatic recordings the field of view was 400 × 400 µm. Images of FB axons were taken 20–100 µm below dura. Images of L2/3 neurons were taken 120–250 µm below dura. Imaging areas for both axons and neurons were mostly located over monocular primary visual cortex (Fig. 2a). The microscope was controlled using ScanImage5[53] (Vidrio). Laser power measured at the objective exit varied between 25 and 35 mW when recording axons and between 60 and 110 mW when recording somata. For each mouse, the objective optical axis was aligned perpendicularly to the imaging window.

**Image analysis.** A trial with visible structure and little movement was selected and averaged across all frames. The average of each trial from an imaging session was registered to this averaged image using a cross-correlation-based fast algorithm[54], and the same shift value was applied to all the frames in the trial. Regions of interest (ROIs) were manually drawn over fluorescent varicosities in the mean projection of the registered session. For somatic V1 recordings, doughnut-shaped ROIs were drawn over cell bodies, excluding nuclei, using a semiautomated procedure[24]. The pixels in each ROI were averaged to estimate the fluorescence corresponding to a single varicosity. The ROI's baseline fluorescence, $F_0$, was estimated at the 30th percentile of fluorescence using a 60-s sliding window. $F_0$ was used to calculate $\Delta F/F_0 = (F - F_0)/F_0$.

**Visual stimulation.** For both the intrinsic signal imaging and the two-photon imaging, visual stimuli were presented using an LED display (BenQ XL2411Z, 144-Hz monitor, stimulus presented at 60 Hz). To ensure that the location of stimulus presentation was consistent across experiments, the monitor was positioned using a custom laser-cut acrylic alignment tool. The alignment tool attached to the headpost holder and extended lateral–anterior over the mouse's head. Aligning fiducial marks on the monitor with the tool allowed positioning the screen reliably in the same place relative to the mouse's right eye, during both intrinsic and two-photon imaging experiments. The screen was positioned 11 cm from the right eye of the animal and oriented at 30° to the axis of the body. This arrangement allowed the presentation of stimuli in a portion of the visual space larger than 120° in azimuth and 60° in elevation. Visual stimuli were generated and presented using Matlab and the Psychophysics Toolbox[55]. For the intrinsic imaging retinotopic mapping of the visual areas, a periodic drifting bar was continuously presented 80 times for each of the four cardinal directions (12-s period, 20° width, masking an alternating checkerboard pattern at 5 Hz). For measuring the RFs of both neurons and axons, a small moving bar was presented inside a 10° by 10° square (2° width, 25°/s speed, 1-s duration intermingled with a 4-s interstimulus interval). The stimulus location was arranged in a 12 by 6 grid covering 120° in azimuth and 60° in elevation (Fig. 1d). In each trial, the bar was presented moving sequentially in the four cardinal directions in a pseudorandom fashion. A total of 10 repetitions were presented in each grid location. For both the retinotopic mapping and the RF stimuli, a spherical correction was applied to compensate for the monitor flatness and visual space was measured in azimuth and elevation coordinates[48]. The same coordinate system was used in both experiments. For measuring the orientation tuning properties of LM axons, full-field sinusoidal drifting gratings with two possible temporal frequencies were presented in eight directions in a pseudorandomized order (0.04 cycles per degree, 1 or 4 Hz, 1-s duration interleaved with a 4-s interstimulus interval, 20 repetitions per stimulus).

**Histology.** After completion of imaging experiments, mice were deeply anaesthetized, transcardially perfused, and fixed overnight with 4% paraformaldehyde in 0.1 M phosphate buffer, pH 7.4. The brain was cut into 50-µm-thick coronal sections with a vibrating slicer (Leica). GCaMP6s$^+$ cells and processes were detected using a polyclonal anti-GFP antibody (ThermoFisher, catalog #A-6455) and an Alexa Fluor 488-conjugated secondary antibody (ThermoFisher, catalog #A-11008) and counterstained with DAPI. We imaged the visual areas at high resolution using a slide scanner with a 20× objective (Axio Scan.Z1, Zeiss) or a confocal microscope with a 40× objective (LSM 710, Zeiss). Retrogradely labeled cell bodies in V1 were mostly absent or extremely rare (Supplementary Fig. 1)

**Data analysis.** All analyses were performed using custom-written code in Matlab.

**Retinotopic maps.** Azimuth and elevation maps of the visual cortical areas were obtained by calculating the phase for each pixel of the discrete Fourier transform at the visual stimulation frequency[23]. Hemodynamic delay was cancelled by subtracting the phase maps of the experiments from opposing moving stimuli. The maps were spatially filtered with a 100 µm radius disk (Fig. 1b, Fig. 2a). For each two-photon imaging session, the center of the imaging location was determined by the local vasculature pattern recorded with a camera. The two-photon imaging field of view was overlaid on top of the retinotopic maps, after rotating and scaling. In both the axonal and somata imaging experiments, the local V1 retinotopy was measured by the filtered intrinsic retinotopic map at the location of the ROI. To measure the extent of the field of view in retinotopic coordinates (filled areas in Fig. 1f), we interpolated the retinotopic maps with the perimeter of the fields of view.

**Receptive fields.** For each ROI, responses at each location were baseline subtracted (baseline: 0.5 s before stimulus onset) and averaged across repetitions. A 12 by 6 map of stimulus responses was obtained by averaging the responses from stimulus onset to 1 s after stimulus offset (2 s total). The stimulus response map $R(az, el)$, where $az$ and $el$ are the retinotopic coordinates azimuth and elevation, respectively, was fitted with a two-dimensional Gaussian curve, using the Matlab implementation of the least-squares Levenberg–Marquardt algorithm:

$$R(az,el) = a + b \cdot exp\left[-\left(\frac{(az-az_0)\cdot cos\theta + (el-el_0)\cdot sin\theta}{\sqrt{2}\cdot\sigma_1}\right)^2 - \left(\frac{-(az-az_0)\cdot sin\theta + (el-el_0)\cdot cos\theta}{\sqrt{2}\cdot\sigma_2}\right)^2\right]$$



© 2018 Nature America Inc., part of Springer Nature. All rights reserved.

where $(az_0, el_0)$ is the center of the 2D Gaussian in azimuth and elevation, $\sigma_1$ and $\sigma_2$ are the s.d. along the two axes of the Gaussian, $\theta$ is the rotation angle of the Gaussian in relation to the azimuth–elevation coordinate system, and $a$ and $b$ are offset and amplitude parameters. The RF boundary was considered to be the ellipse defined by the center $(az_0, el_0)$ and the s.d. of the fitted 2D Gaussian (Figs. 1d and 2c):

$$\left[\left(\frac{(az-az_0)\cdot cos\theta+(el-el_0)\cdot sin\theta}{\sigma_1}\right)^2+\left(\frac{-(az-az_0)\cdot sin\theta+(el-el_0)\cdot cos\theta}{\sigma_2}\right)^2\right]=1$$

Only fits with $R^2 > 0.5$ and s.d. between 5° and 50° were considered in the analysis. Fits with lower $R^2$ were dominated by unreliable estimates of RF position and shape.

**Calibration of intrinsic maps of V1 retinotopy.** We measured how the RFs of individual L2/3 V1 neurons related to the retinotopic map measured with intrinsic imaging (Fig. 2). These measurements also allowed calibrating retinotopic maps obtained with ISI to better reflect the average RF of L2/3 neurons. We performed a linear fit between the two-photon RFs and the intrinsic retinotopy discarding the borders of the stimulus space ($azimuth_{ISI}$ in [−45°, 45°] and $elevation_{ISI}$ in [−15°, 15°]), obtaining the following relationships: $azimuth_{2P} = 1.14 \times azimuth_{ISI} + 3.34$, and $elevation_{2P} = 0.84 \times elevation_{ISI} - 2.04$. These equations were used to correct the intrinsic maps of V1 retinotopy in all the data.

**Probability distribution of the relative retinotopy.** We define the relative retinotopic position of the LM boutons or V1 somata as the difference between the centers of their RFs, measured in the two-photon imaging experiments ($RF_{2P}$), and the calibrated local retinotopy in V1 of the ROI, measured using intrinsic imaging ($V1_{ISI}$)

$$\Delta\mathrm{RF} = RF_{2P} - V1_{ISI}$$

with components

$$\Delta\mathrm{Azimuth} = \mathrm{azimuth}(\mathrm{RF}_{2P}) - \mathrm{azimuth}(V1_{ISI})$$

$$\Delta\mathrm{Elevation} = \mathrm{elevation}(RF_{2P}) - \mathrm{elevation}(V1_{ISI})$$

Our data is bounded by the visual space covered by the stimulus ([−60°, 60°] in azimuth and [−30°, 30°] in elevation). As a consequence, not all values of ΔRF are equally sampled. While ROIs with ΔAzimuth = 0 can potentially be observed when the two-photon field of view is positioned over any location in V1, those with ΔAzimuth = −120° can only be observed when recording at V1 locations with azimuth values of 60°. Similarly, ROIs with ΔElevation = 0 can potentially be observed when the field of view is over any location in V1, while those with ΔElevation = −60 ° can only be observed when recording at V1 locations with elevation values of 30°. This can be visualized by measuring the length of lines parallel to the identity line in Fig. 3a, bounded by the square region of the plot. The length is largest at the identity line (ΔElevation or ΔAzimuth equal to 0) and linearly decreases as it moves further away, becoming null at the extremes. To obtain an unbiased probability distribution of ΔRF, we introduced a sampling weight corresponding to the inverse of the relative probability of sampling a given ΔRF:

$$w(\Delta az, \Delta el) = \left(1 - \frac{|\Delta az|}{max(\Delta az)}\right)^{-1} \cdot \left(1 - \frac{|\Delta el|}{max(\Delta el)}\right)^{-1}$$

where $w$ is the sampling weight, $\Delta az$ and $\Delta el$ are ΔAzimuth and ΔElevation and $max(\Delta az)$ and $max(\Delta el)$ are the maximum possible deviations measured for azimuth and elevation (120° and 60° respectively). Thus, $w = 1$ for a ROI with ΔRF = 0, and $w > 1$ for any given deviation. The ΔRF probability distributions in Fig. 4 represent weighted distributions of the sampled data (5 × 5° bins).

To calculate the spatial coverage probability map (Fig. 4d), we performed a weighted mean of all the elliptical RF fits in relative retinotopic coordinates. As before, RFs were weighted depending on the ΔAzimuth and ΔElevation of their centers to correct sampling biases. Thus, Fig. 4d reflects the probability that a given position in relative visual space is represented by one converging LM FB input.

We calculated the relative retinotopic distance ‖ΔRF‖ in Fig. 4 as

$$\|\Delta\mathrm{RF}\| = \sqrt{\Delta az^2 + \Delta el^2}$$

We quantified the local scattering of L2/3 V1 neurons as the geometric mean of the s.d. of the ΔRF along the two axes:

$$Local\ \ Scattering = \sqrt{std(\Delta az)\cdot std(\Delta el)}$$

We obtained a value of local scattering for each mouse. The differences in V1 RF positions relative to the ISI retinotopic map were similar to the known local scatter of L2/3 RFs in mouse V1[29,30] (Fig. 2e,f; scatter around intrinsic value = 7.1 ± 1.7°, 4 mice).

To calculate the relative retinotopic distance of V1 dendrites (Fig. 4c), we shifted the relative retinotopic position of each V1 neuron by a displacement vector sampled from a uniform distribution within a circle of 15° radius (range of apical dendritic arborization, assuming 300-µm wide dendritic trees in L1). The cumulative distribution of relative retinotopic distance in Fig. 4c represents the mean of 10,000 simulations.

**Feedback RF overlap.** We calculated the amount of overlap between the RFs of L2/3 V1 neurons and LM boutons (Fig. 4f) by sampling from the ΔRF probability distributions of LM bouton and V1 somata RF centers. For each pair of RFs (formed by one V1 neuron and one LM bouton), the overlap was defined as the shared area between the two divided by the area of the V1 RF (10,000 iterations).

Additionally, we considered the fact that the retinotopic position of the dendrites of V1 neurons may deviate from the position of their soma when calculating the amount of overlap between the RFs (Fig. 4f). To do so, we repeated the same procedure as before but shifted the RF of the V1 neuron by a displacement vector sampled from a uniform distribution within a circle of 15° radius, assuming 300-µm wide dendritic trees.

**Feedback aggregate RF.** To estimate the aggregate RF of the LM FB to a V1 neuron (Fig. 4g) we sampled $n$ LM boutons from the ΔRF probability distribution with replacement 10,000 times. For each sample we calculated the aggregate RF as the area defined by the outer boundary of the RF elliptical fits of the $n$ boutons.

Since LM boutons can contact V1 neurons in any of their dendritic branches in L1, we estimated the effect of the number of branches in the size of the aggregate RF. For this we simulated individual branches as sampling points displaced from retinotopic positions of the somata. To do so we introduced a displacement in the LM ΔRF probability distribution sampled from a uniform distribution within a circle of 15° radius for each branch.

**Analysis of tuning properties of LM boutons.** We measured tuning properties of LM boutons in 37 of 45 sessions. For each ROI, $\Delta F/F_0$ traces were averaged over all repetitions for each stimulus type, after subtracting the baseline fluorescence during the 0.5 s before stimulus presentation (Figs. 5a and 6a). The mean stimulus response was obtained by averaging the mean fluorescence trace between the stimulus onset and 1 s after stimulus offset (2 s total). Tuning properties were measured only for the temporal frequency that elicited the largest response. The response for each orientation was obtained by averaging the responses to two opposing directions. The preferred orientation was determined as the one that corresponded to the maximum orientation response. Analogously, the preferred direction was determined as the one that corresponded to the maximum response. A signal-to-noise ratio (SNR) was calculated as:

$$SNR = \frac{R^{Dir}_{pref}}{\sigma}$$

where σ is the mean of the s.d. of the fluorescence trace during the baseline period (0.5 s before the stimulus presentation) for each trial and $R^{Dir}_{pref}$ is the mean response to the preferred direction. Only ROIs with SNR > 0.5 were considered to be reliably driven by the grating stimulus and included in the analysis. ROIs were considered to be orientation-selective (OS) if their responses to the preferred orientation were significantly larger than to the orthogonal orientation ($P < 0.05$ for a two-sample $t$ test). Similarly, ROIs were considered direction-selective (DS) if the responses to the preferred direction were significantly larger than to the opposite direction ($P < 0.05$ for a two-sample $t$ test). Boutons were considered nonselective if they were either nonresponsive to any moving grating or responsive but neither OS nor DS.

We quantified how selective LM boutons were by calculating an orientation-selective index (OSI) and a direction-selective index (DSI) according to:

$$OSI = \frac{R^{Or}_{pref} - R^{Or}_{orth}}{R^{Or}_{pref} + R^{Or}_{orth}} \qquad DSI = \frac{R^{Dir}_{pref} - R^{Dir}_{opp}}{R^{Dir}_{pref} + R^{Dir}_{opp}}$$

where $R^{Or}_{pref}$ is the mean response to the preferred orientation, $R^{Or}_{orth}$ to the orthogonal orientation, and $R^{Dir}_{opp}$ to the direction opposite to the preferred.

**Angular distribution of relative retinotopy.** We calculated the angular distribution of the deviation angle, θ, by dividing the plane defined by ΔAzimuth and ΔElevation in eight bins of 45° (Fig. 5c). We discarded ROIs with a ‖ΔRF‖ of less than 10° due to the imprecise nature of angular measurements close to the origin of a coordinate system. We counted the number of LM boutons in each angular bin (Supplementary Fig. 4). To compare the angular distributions of the different populations of OS and DS LM boutons we normalized them by dividing by the angular distribution of the nonselective boutons (Figs. 5d and 6c).



© 2018 Nature America Inc., part of Springer Nature. All rights reserved.

To measure how the deviation angle θ relates to the preferred orientation of OS LM boutons, we counted the number of boutons in four bowtie bins (one perpendicular, one parallel, and two oblique to the preferred orientation). For each OS subpopulation, we normalized the bowtie angular counts by dividing by those of the nonselective boutons (Fig. 5g). To calculate the mean normalized counts, we averaged the values across the four different OS subpopulations, weighted by the number of boutons in each group (Fig. 5h). We show the non-normalized bowtie angular counts in Supplementary Fig. 4 to measure the absolute differences in boutons counts across bins.

For the DS boutons, we calculated the normalized angular distributions of θ using, as reference, the angle of the preferred direction (Fig. 6e). We then averaged the normalized angular distributions across the eight different DS subpopulations, weighted by the number of boutons in each group (Fig. 6f).

In Fig. 5j, we measured the difference between the ΔRF probabilities of OS and nonselective boutons. First, we calculated the 2D probability of ΔRF for each OS subpopulation as in Fig. 4b and subtracted from it the values of the nonselective boutons. We then rotated each spatial coverage probability difference map by the angle of the groups' preferred orientation and by the preferred orientation + 180°. The values of the eight maps were averaged in 20 × 20° bins, weighted by the number of boutons in each group. We performed a similar analysis for DS boutons (Fig. 6h), but rotating the 2D probability-of-ΔRF-differences map of each DS subpopulation by its preferred direction. To estimate differences in visual coverage (Figs. 5j and 6h), we performed similar analyses but averaging the elliptical fits of the RFs, as in Fig. 4d.

**Determination of boutons' axonal identity.** Several boutons in the same field of view can be part of the same LM axon. In all our analyses, we included boutons independently of their axonal identity. However, statistical tests assume independence of samples, which is not true when boutons belong to the same axon. Thus, we identified boutons as belonging to the same axons when performing permutation tests (see below). First we selected boutons in the same session that were clearly part of the same axon (Supplementary Fig. 2) by visual inspection, as they were connected by a visible axonal shaft when averaging all the frames in a session.

We computed the correlation coefficient (Pearson's, *R*) for each pair over the entire session for the RF stimulus and compared them to the correlation coefficients over all pairs (Supplementary Fig. 2). As expected, pairs that belonged to the same axon had higher correlation coefficients than random pairs[10], 97% of them showing $R > 0.35$ (compared to only 0.2% of all pairs). Given this, we considered pairs as candidates to belonging to the same axon if their responses showed a correlation coefficient $R > 0.35$. We then looked at the difference between the centers of the RFs for each pair. Boutons that belonged to the same axon showed overlapping RFs with small differences in the positions of their centers (96% < 5° away; Supplementary Fig. 2). Therefore, we required boutons to have distances between the centers of their RFs of less than 5° to be considered as belonging to the same axon. Finally, we required boutons to have the same selectivity when considering the responses to the moving gratings. If a pair of boutons satisfied these three criteria, it was considered to be part of the same axon, even if a physical link between them could not be visually discerned.

To determine axonal identity in a given session we selected all the pairs that were considered to be from the same axon. We seeded an axon with one pair. We then started adding pairs that shared one of the ROIs with the existing axon until there were no more pairs that satisfied this condition. Then we seeded another axon with an unassigned pair and repeated the procedure until all pairs had been assigned[10]. We found that for 12% of all recorded boutons, there was at least another bouton from the same axon in the field of view.

**Statistical analyses.** No statistical tests were used to predetermine sample sizes. Sample sizes are similar to those in previous studies[25]. All values in the text are presented as mean ± s.d. Statistical analyses were performed in Matlab with the functions for the tests specified (ranksum, kstest2, regress, and ttest2) and with resampling tests using custom-written code. *P* values were obtained with two-sided tests and adjusted for multiple comparisons using the Bonferroni–Holm correction. Most analyses relied on nonparametric or resampling tests that do not assume normality of the data distributions. When testing the significance of the linear regressions in Figs. 2e and 3a, we checked the normality of the residuals using a one-sample Kolmogorov–Smirnov test.

To determine whether the RF positions of the LM boutons depended on the position in V1 where they were recorded, we ran a permutation test (10,000 iterations) under the null hypothesis that these variables were independent (Fig. 3b). Thus, for each iteration, we shuffled the V1 retinotopy values across the LM boutons, taking into account their axonal identity, and calculated the distribution of ΔAzimuth and ΔElevation. We then compared the 95% confidence intervals of these distributions to the observed distributions. We performed a similar analysis for V1 neurons (Fig. 2f). To test that the distribution of relative retinotopic distance of LM boutons had a larger median than V1 dendrites (Fig. 4b), we performed a permutation test (10,000 iterations), taking into account the axonal identity of the boutons. For each iteration, we shuffled the relative retinotopic distance of LM axons and their assigned boutons with those of V1 dendrites.

To test that the distribution of preferred orientation of OS boutons was not uniform (Fig. 5b), we performed a resampling test (5,000 iterations), taking into account the axonal identity of the boutons. For each iteration, we assigned a random preferred orientation to each OS axon and all the boutons that were considered part of it, with equal probability. Then we counted the number of boutons in each OS group, obtaining a distribution of preferred orientations. We then compared the 95% confidence interval of these simulated distributions to the observed one. To test that the distribution of preferred direction of DS boutons was not uniform, we performed an analogous test but now randomly assigned preferred directions to DS axons (Fig. 6b).

To test whether the angular distribution of the deviation angle, θ, was enriched in the orientation perpendicular to the preferred orientation of the OS boutons (Fig. 5h,i), we performed a permutation test, taking into account the axonal identity of the LM boutons (5,000 iterations). For each iteration, we shuffled the axons and its assigned boutons between the five different groups (each OS subpopulation and the nonselective population). We obtained a simulated distribution of normalized bowtie angular counts of ΔRF as well as the difference between perpendicularly oriented bins. We then compared the 95% confidence interval of these distributions to the values measured (Fig. 5h,i). To obtain the *P* values, we calculated the probability of obtaining a value equal or larger than our measurements in the simulated distributions (using a two-sided test). We then corrected the *P* values using the Bonferroni–Holm method, taking into account the number of comparisons we made (four for the normalized bowtie angular counts and two for the difference between perpendicularly oriented bowtie bins).

To test whether the angular distribution of θ for DS boutons was more enriched in the preferred direction than in the opposite direction (Fig. 6f,g), we used a permutation test similar to the one described for the OS boutons, taking into account the axonal identity of the DS boutons. We simulated normalized distributions of θ, as well as the difference between bins corresponding to opposing directions for DS boutons. We then compared the 95% confidence intervals of these distributions to the ones measured (Fig. 6f,g) and calculated the *P* values using a two-sided test and correcting for multiple comparisons (four for the difference between opposing directions bins).

To see how the biases in the angular distributions varied with relative retinotopic distance, we performed analyses identical to the ones described for both the OS and DS boutons in five equally populated ||ΔRF|| bins (Supplementary Fig. 5).

To test whether the normalized bouton count difference between the perpendicular and parallel bowtie bins depended on the boutons' orientation selectivity, we considered all boutons that were responsive to the gratings stimuli and divided them in four equally populated OSI bins (Supplementary Fig. 5). Then, for each bin we calculated the difference in bouton abundance between the perpendicular and parallel bowtie bins and determined the slope of the linear regression between count difference and OSI. We performed a permutation test by shuffling the values of OSI, taking into account the axonal identity of the boutons, and determining the probability of getting the observed value by chance (10,000 repetitions). We performed a similar analysis to test whether the difference in bouton abundance between the preferred motion direction and opposite bins depended on the boutons' DSI (Supplementary Fig. 5).

**Reporting Summary.** Further information on experimental design is available in the Nature Research Reporting Summary.

**Data and code availability statement.** The data and code that support the findings of this study are available from the corresponding author upon reasonable request.

## References

51. Dana, H. et al. Thy1-GCaMP6 transgenic mice for neuronal population imaging in vivo. *PLoS One* **9**, e108697 (2014).
52. Suter, B. A. B. A. et al. Ephus: multipurpose data acquisition software for neuroscience experiments. *Front. Neural Circuits* **4**, 100 (2010).
53. Pologruto, T. A., Sabatini, B. L. & Svoboda, K. ScanImage: flexible software for operating laser scanning microscopes. *Biomed. Eng. Online* **2**, 13 (2003).
54. Guizar-Sicairos, M., Thurman, S. T. & Fienup, J. R. Efficient subpixel image registration algorithms. *Opt. Lett.* **33**, 156–158 (2008).
55. Brainard, D. H. The Psychophysics Toolbox. *Spat. Vis.* **10**, 433–436 (1997).



© 2018 Nature America Inc., part of Springer Nature. All rights reserved.

nature research

Corresponding author(s): Leopoldo Petreanu

# Reporting Summary

Nature Research wishes to improve the reproducibility of the work that we publish. This form provides structure for consistency and transparency in reporting. For further information on Nature Research policies, see Authors & Referees and the Editorial Policy Checklist.

## Statistical parameters

When statistical analyses are reported, confirm that the following items are present in the relevant location (e.g. figure legend, table legend, main text, or Methods section).

| n/a | Confirmed | |
|---|---|---|
| ☐ | ☒ | The exact sample size (*n*) for each experimental group/condition, given as a discrete number and unit of measurement |
| ☐ | ☒ | An indication of whether measurements were taken from distinct samples or whether the same sample was measured repeatedly |
| ☐ | ☒ | The statistical test(s) used AND whether they are one- or two-sided<br>*Only common tests should be described solely by name; describe more complex techniques in the Methods section.* |
| ☒ | ☐ | A description of all covariates tested |
| ☐ | ☒ | A description of any assumptions or corrections, such as tests of normality and adjustment for multiple comparisons |
| ☐ | ☒ | A full description of the statistics including central tendency (e.g. means) or other basic estimates (e.g. regression coefficient) AND variation (e.g. standard deviation) or associated estimates of uncertainty (e.g. confidence intervals) |
| ☐ | ☒ | For null hypothesis testing, the test statistic (e.g. *F*, *t*, *r*) with confidence intervals, effect sizes, degrees of freedom and *P* value noted<br>*Give P values as exact values whenever suitable.* |
| ☒ | ☐ | For Bayesian analysis, information on the choice of priors and Markov chain Monte Carlo settings |
| ☒ | ☐ | For hierarchical and complex designs, identification of the appropriate level for tests and full reporting of outcomes |
| ☐ | ☒ | Estimates of effect sizes (e.g. Cohen's *d*, Pearson's *r*), indicating how they were calculated |
| ☐ | ☒ | Clearly defined error bars<br>*State explicitly what error bars represent (e.g. SD, SE, CI)* |

*Our web collection on statistics for biologists may be useful.*

## Software and code

Policy information about availability of computer code

| | |
|---|---|
| Data collection | ScanImage 5 , Psychtoolbox-3 |
| Data analysis | Custom code in Matlab |

For manuscripts utilizing custom algorithms or software that are central to the research but not yet described in published literature, software must be made available to editors/reviewers upon request. We strongly encourage code deposition in a community repository (e.g. GitHub). See the Nature Research guidelines for submitting code & software for further information.

## Data

Policy information about availability of data

All manuscripts must include a data availability statement. This statement should provide the following information, where applicable:

- Accession codes, unique identifiers, or web links for publicly available datasets
- A list of figures that have associated raw data
- A description of any restrictions on data availability

Data is available from the corresponding author upon request

# Field-specific reporting

Please select the best fit for your research. If you are not sure, read the appropriate sections before making your selection.

☒ Life sciences ☐ Behavioural & social sciences

For a reference copy of the document with all sections, see nature.com/authors/policies/ReportingSummary-flat.pdf

# Life sciences

## Study design

All studies must disclose on these points even when the disclosure is negative.

| | |
|---|---|
| Sample size | No statistical tests were used to predetermine sample sizes. Sample sizes are similar to those in previous studies. |
| Data exclusions | In all analyses we only included boutons with good RF fits. Boutons with RF Gaussian fits with R^2<0.5 or SDs that were <5 deg or >50 deg were excluded from analysis. The criterion was determined after data collection to exclude unreliable fits. |
| Replication | Given biological variability, our study is designed to measure population data from large numbers of axonal boutons. All the measurements rely on population analysis of data obtained from 45 independently-sampled imaging locations across 5 animals. All data was pooled together. No attempts were made to replicate the population data. |
| Randomization | There were no allocated experimental groups in this study. Bouton tuning groups are defined by their properties. |
| Blinding | There were no allocated experimental groups in this study. |

## Materials & experimental systems

Policy information about availability of materials

| n/a | Involved in the study |
|---|---|
| ☒ | ☐ Unique materials |
| ☐ | ☒ Antibodies |
| ☒ | ☐ Eukaryotic cell lines |
| ☐ | ☒ Research animals |
| ☒ | ☐ Human research participants |

### Antibodies

| | |
|---|---|
| Antibodies used | anti- GFP antibody (ThermoFisher, Catalog# A-6455)<br>Alexa 488 –conjugated secondary antibody (ThermoFisher, Catalog# A-11008) |
| Validation | The validation of these antibodies was provided from the companies that provided the antibodies. |

### Research animals

Policy information about studies involving animals; ARRIVE guidelines recommended for reporting animal research

| | |
|---|---|
| Animals/animal-derived materials | Wild-type male C57BL/6J mice were used for in vivo functional imaging of LM feedback axons. L2/3 somata in V1 were imaged in one Thy1-GCaMP6s GP4.3 51 (Jax Stock No: 024275) and three C57BL/6J male mice . Mice were individually housed in a reversed lightdark cycle and had ad libitum access to food and water and were only used for the experiments reported here. Animals were 8-10 week old at the start of the experiments |

# Method-specific reporting

| n/a | Involved in the study |
|---|---|
| ☒ | ☐ ChIP-seq |
| ☒ | ☐ Flow cytometry |
| ☒ | ☐ Magnetic resonance imaging |